

Al_2O_3 -MnS Inclusions and Pitting Corrosion in the Weld Heat-Affected Zone

An explanation for the selective reactivity of sulfides suggests that only those clustering with oxides will function as active pitting initiation sites

BY Y. WANG, Z. LYU, Z. WU, AND L. LI

Abstract

Manganese sulfide inclusions have been identified as a key factor contributing to the degradation of pitting corrosion resistance in both carbon and stainless steels. However, the precise reasons behind the differential reactivity of various sulfides, with some serving as active sites for pitting while others remain inactive, are not yet fully understood. The effect of debonding occurring at the interface between these inclusions and the steel matrix in relation to pitting corrosion has not been extensively investigated. In this study, an examination of a service-exposed pipeline girth weld was conducted. Immersion testing in blowdown water and multi-scale characterization techniques investigated the inclusion-matrix interface debonding within the heat-affected zone. Our findings suggest that interfacial debonding is more likely at the Al_2O_3 -MnS cluster interface. This observation offers a rationale for the selective reactivity of sulfides that form clusters with oxides, highlighting the likelihood that only sulfides clustering with oxides act as active pitting initiation sites.

Keywords

- FAC
- Girth Weld
- Al_2O_3
- MnS
- Pits Initiation
- Interfacial Debonding

Introduction

Low-carbon micro-alloyed steels, serving as a crucial structural material, are widely used in industrial applications owing to their cost-effectiveness, mechanical properties, and weldability (Refs. 1–3). Numerous studies have highlighted the significant impact of flow-accelerated corrosion (FAC) on carbon steel and stainless-steel steam pipes, contributing to premature failures resulting in substantial economic losses (Refs. 4–8).

FAC-induced damage has been frequently identified in structural components featuring geometric irregularities, such as pipe bends, tube constrictions, tee joints, and other elements causing sudden changes in flow direction or velocity (Refs. 9, 10). Regrettably, there has been a lack of adequate attention paid to FAC damage in steam pipe girth welds. Prior investigations of FAC have mainly focused on the relationship between component FAC damage and service environments, such as fluid chemistry (temperature, pH level, dissolved oxygen, etc.) and flow pattern (component configuration, etc.) (Refs. 11–14). However, explaining the FAC mechanism from a metallurgical point of view has not been pursued thoroughly. Tomarov et al. (Ref. 15) have categorized FAC into two distinct types: general flow-accelerated corrosion (GFAC) and local flow-accelerated corrosion (LFAC). GFAC is most frequently observed and is characterized by a moderate rate of uniform metal thinning that typically does not lead to pinholes compromising the integrity of the circuit. On the contrary, LFAC is less frequently observed and is characterized by significant metal thinning in a localized area, potentially resulting in the formation of wormholes for sudden pipeline damage. LFAC is often associated with girth welds.

Pitting damage may occur when the flow in a piping system contains aggressive ions, such as chloride and sulfide. The weld components are at a higher risk of pitting attack, particularly in high temperatures and with chemical and microstructural heterogeneity. Fredj et al. (Ref. 16) suggested that the chemical nature of the water is a critical

parameter that increases susceptibility to pitting for mild steel, regardless of the velocity of flow or the duration of immersion. Additionally, Karaminezhaad-Ranjbar et al. (Ref. 17) proposed that flow velocity has minimal effect on the process of pit nucleation on Inconel 600 in a 0.1 M NaCl solution across a wide range of temperatures (25 to 250°C). Although fluid motion does exert some influence over pit morphology, surface inhomogeneities and temperature are the dominant factors affecting pitting attacks. In our previous work (Ref. 18), pitting damage was defined as the precursor of localized corrosion damage that synergistically affects the FAC process of a girth weld in a steam pipe in conjunction with dynamic flow erosion.

Generally, manganese was intentionally added to steels as a sulfur scavenger to form manganese sulfide in preference to FeS, which formed low-melting point grain boundary liquid films, leading to hot shortness, thus eliminating the harmful effect of eutectic FeS. For decades, it was accepted that MnS inclusions were the most decisive factor for deteriorating pitting corrosion resistance for carbon or stainless steel (Refs. 19–23). While abundant effort was made to pursue the mechanism of inclusion-induced pitting damage in various grades of stainless steels, a comprehensive understanding of pitting initiation in carbon steels was missing.

Regarding the mechanism of pitting initiation, it has been widely accepted that Cl⁻ is a contributor of pitting initiation because it can catalyze the dissolution of iron and, thus, accelerate the corrosion reaction; at the same time, chloride can destroy the continuity of protective oxide film, making the oxide layer more easily removed from the metal surface (Refs. 24–26). Besides, sulfide inclusion is found to be the preferred location for pitting. Yet it remains unclear why certain sulfides are active sites for pitting initiation, whereas others are deemed inactive. Because the linear thermal expansion coefficient of MnS is greater than that of ferrite (Ref. 27), when the interface bonding strength is not enough to withstand the stress caused by the thermal deformation, inclusion/matrix debonding may occur.

In addition to causing anisotropic mechanical properties, elongated manganese sulfides and MnS/Al₂O₃ clusters were frequently observed to be related to a brittle intergranular fracture (Refs. 28–30). Mechanical properties could also be impaired due to the interfacial debonding of the MnS inclusion and steel matrix (Ref. 31). Glue et al. (Ref. 29) have proposed that due to overheating, the original α-MnS particles in low-alloy steels dissolve into the matrix during the initial high-temperature treatment. Subsequently, the sulfides reprecipitate at austenite grain boundaries after cooling through the overheating range. They have also observed that intergranular grain boundary separation is associated with microvoid coalescence at the inclusions/matrix interface. This study demonstrates that microvoids or crevices arising from inclusion/matrix interfacial debonding may be an additional factor contributing to pitting initiation in low-carbon piping steel.

Experimental Procedure

Pipeline sections featuring reduced wall thickness and cavity-like damage on the inner surface were procured from

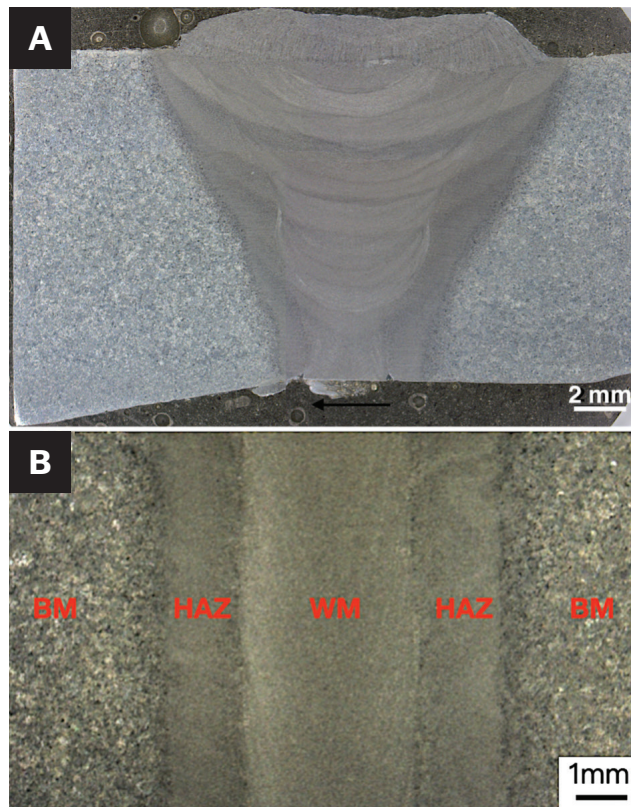


Fig. 1 — A — Macrograph of the girth weld near the nine o'clock location, showing the weld root reinforcement removed by erosion-corrosion; B — macrograph of an internal diameter specimen, showing the surface of the weld root joint. Once polished, the specimen is ready for corrosion immersion testing.

a steam distribution pipeline. The pipe material utilized was CSA Z245.1 Grade 550 low-carbon steel, characterized by a composition of 0.09 wt-% C, 0.02 wt-% Cr, 1.41 wt-% Mn, 0.038 wt-% Ni, 0.097 wt-% Mo, 0.274 wt-% Si, 0.003 wt-% S, and 0.01 wt-% P. The weld root pass was executed using an E6010 electrode by shielded metal arc welding with a heat input of 34 kJ/in. Subsequently, filling and cap passes were achieved using E8010 electrodes through flux-cored arc welding with a heat input of 57 kJ/in. A minimum preheating temperature of 150°C was maintained. These girth welds were fabricated per a welding procedure specification that complied with ASME Section IX. The service conditions of the considered piping system included a temperature range of 300 to 380°C, with steam flow velocities ranging from 5 to 30 m/s. This study is a follow-up of a failure analysis of premature damage by flow-accelerated pitting corrosion, an accelerated, localized pitting attack that leads to premature leakage of a steam pipe. The acceleration is due to fluid flow; pitting is the corrosion mechanism for FAC. To enable a detailed study of inclusions and pitting, the service-exposed girth welds were polished and exposed to the same blowdown water for corrosion testing.

Samples underwent mounting, grinding, and polishing for metallographic examinations using the conventional mechanical method, and grinding involved the application of #180,

Table 1 – Industrial Blowdown Water Chemistry Involved in the Corrosion Tests

Species	Na (g/L)	Cl (g/L)	S (g/L)	P (g/L)	Total Carbon (g/L)	pH value
Content	2.11	0.731	0.297	<0.002	1.96	11.23

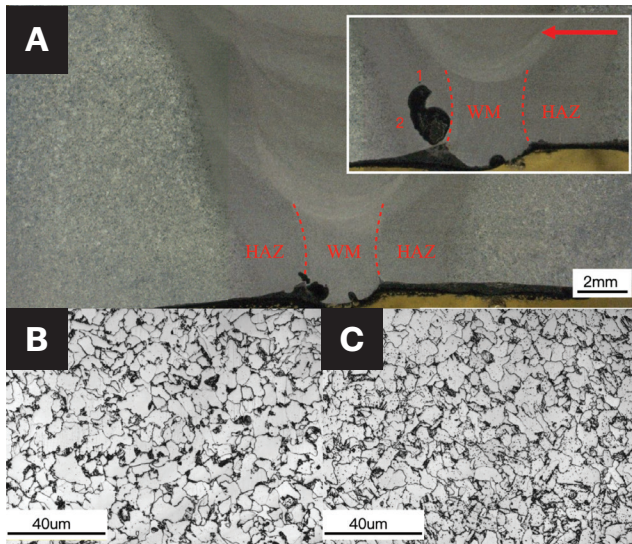


Fig. 2 – A – Morphology of crater damage in the downstream weld toe area of the root pass. The fluid flow direction is from right to left; B – microstructure of Location 1; C – microstructure of Location 2 of the inset. The orientation of the specimen in A is near seven o'clock (i.e., at the bottom of the girth weld circle if the observer is looking down the flow direction).

#360, #600, and #1200 SiC sandpapers followed by polishing with 3.0 μm , 1.0 μm , and 0.5 μm diamond suspensions to achieve scratch-free and mirror-like surfaces. A 4% nital solution served as the surface etching agent. Macro- and micro-scaled morphologies were observed using the ZEISS Stemi 508 stereomicroscope and the Olympus OLS3000 confocal laser scanning microscope (CLSM). The CLSM was also employed to measure corrosion pit depth profiles, providing rapid, accurate, and non-contact surface topography measurements.

Accelerated corrosion immersion tests involved the polished internal diameter surface specimens shown in Fig. 1 and individual mounting of subregion samples (BM [base metal], HAZ [heat-affected zone], and WM [weld metal]) in epoxy, with conductive copper wires attached for electrical connection. Before immersion, scratch-free surfaces were ensured through standard mechanical grinding and polishing. The working electrode surface's interface with epoxy was sealed with silicone rubber to prevent crevice corrosion. Blowdown water, whose chemical composition is shown in Table 1, was used as the immersion test solution. All immersion tests were conducted under ambient temperature in industrial blowdown water, utilizing an Interface 1010E potentiostat from Gamry Instruments. For the observation

of nascent corrosion pits, accelerated corrosion immersion tests were conducted over a potential range from -0.25 V to $+0.25\text{ V}$ against the open circuit potential (OCP) at a scanning rate of 0.5 mV/sec. A three-electrode configuration was used: a standard saturated Ag/AgCl reference electrode, a graphite rod counter electrode, and a specimen serving as the working electrode. A luggin capillary tube was placed close to the working electrode surface to ensure good electrochemical contact with the other electrodes and minimize ohmic potential drop. Before polarization, a stable OCP was established within two hours for each sample. During the test, the electrolyte was exposed to air. After the immersion tests, specimens underwent degreasing in acetone and immersion in analytical pure alcohol for 1 h of ultrasonic cleaning to remove corrosion products and contaminants. Each experiment group underwent at least three repetitions for repeatability, with only representative results presented for comparative analysis.

Pre- and post-immersion tests involved high-resolution morphological and chemical analyses using ZEISS Sigma field emission scanning electron microscopy (FE-SEM) equipped with energy dispersive x-ray spectroscopy (EDS) for detecting characteristic x-ray signals. Electron backscatter diffraction (EBSD) characterizations were also performed in the same FE-SEM vacuum chamber interfacing with a Nordlys EBSD detector from Oxford Instruments. A step size of 0.25 μm was adopted during data acquisition, and post-processing of EBSD data was accomplished through the open-source MATLAB toolbox MTEX. Additionally, a ZEISS Orion helium ion microscope equipped with a gallium-focused ion beam (FIB) was utilized for site-specific inclusion cross-sectional micro-machining, boasting an ultra-high resolution of 0.5 nm.

Results

Figure 2 shows macrographs and the microstructure of the weld-root flow-accelerated corrosion (FAC) damage. The craters are at the weld toe of the downstream side of the weld root, with the arrow indicating the steam/water flow direction. Due to the nonuniform distribution of the two-phase flow field in the cross section of the steam pipe, FAC morphologies are different along the circumferential girth weld. For positional reference, six o'clock designates the bottom while 12 o'clock designates the top of the girth weld circle, assuming the observer is looking in the pipe flow direction. The microstructure, shown in Figs. 2B and C, for Locations 1 and 2, correspond to the area that has been significantly damaged and the area that has been less damaged, respectively. The damage was found to preferentially propagate in the heat-affected zone rather than affecting the base metal. Notably, the coarse-grained heat-affected

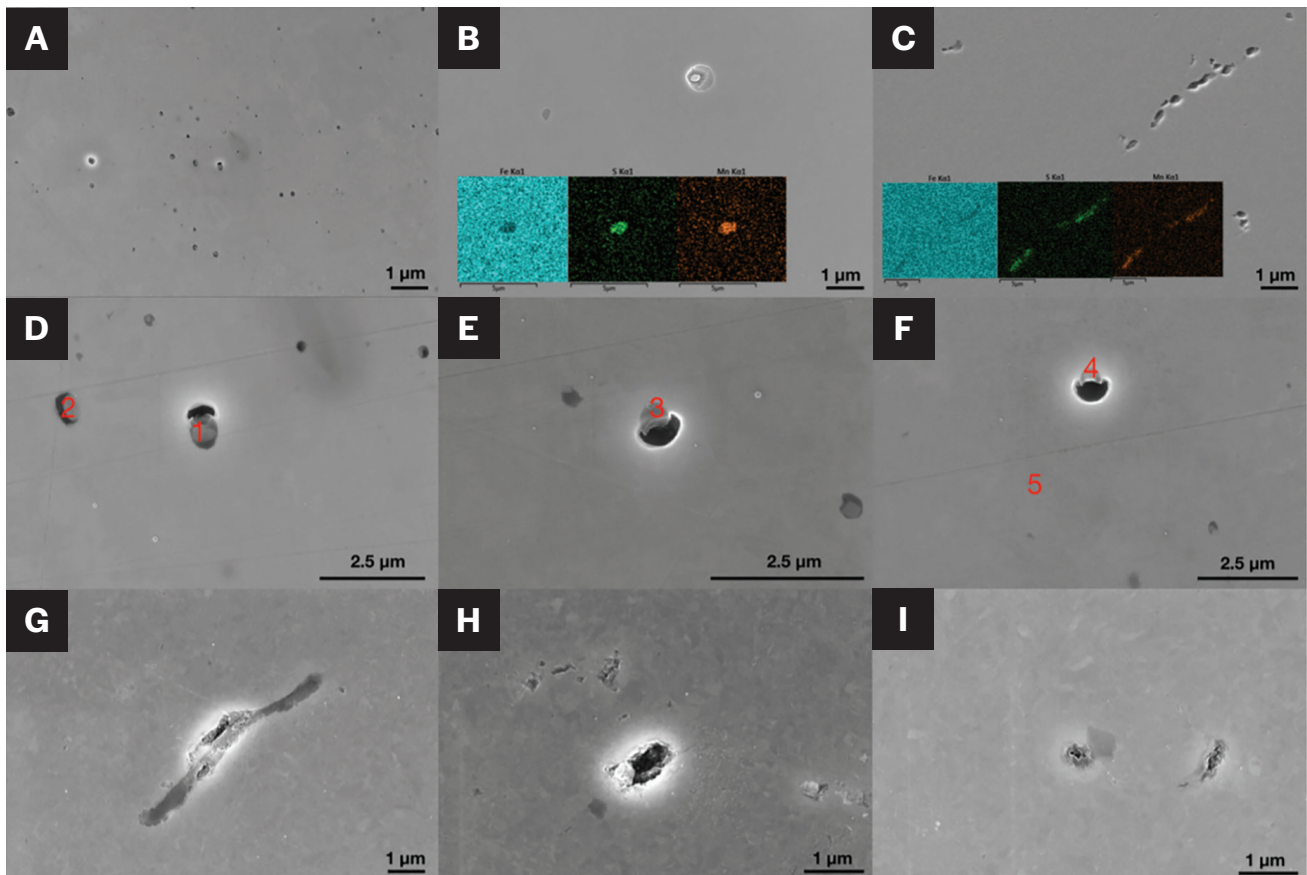


Fig. 3 – Morphology of inclusions and interfacial debonding in different weld subregions: A – Weld root pass weld metal; B – the base metal; C – the heat-affected zone; D–F – the magnified images of the weld root pass metal; G–I – the magnified images of the heat-affected zone.

zone (CGHAZ) close to Location 1 appeared to be more susceptible than the fine-grained heat-affected zone (FGHAZ) close to Location 2.

Corrosion immersion test results on the polished weld root specimens are presented in Table 2. The surface of the weld root joint exhibited pinhole-sized pitting damage. The weld root metal displayed the relatively smallest pitting density, followed by the base metal. The HAZ had the most pitting damage. These results agreed well with the electrochemical experiment data obtained previously (Ref. 18).

Inclusions were observed using the SEM secondary electron imaging mode from the as-polished weld root specimens before immersion testing. Numerous areas in each weld region were observed and documented during the investigation. Representative figures for the WM (Fig. 3A) revealed fine and densely distributed small, round inclusions. Most inclusions in the root pass filler metal were smaller than 0.5 μm, with only a few larger inclusions (0.7–0.9 μm). The enlarged inclusion images for the WM (Figs. 3D and F) show the spherical shapes, debonding, and cavities around the inclusions. The corresponding EDS point analysis results are shown in Table 3. Positions 1 to 4 had a higher concentration of manganese, sulfur, aluminum, and oxygen at inclusion sites. Position 5 is for comparison to the surrounding ferrite matrix. Given that MnS typically appears white-gray under microscopic observation, it is reasonable

to suggest that the weld root metal predominantly contained globular submicron MnS/AlxOy/SiOx complex inclusions. In contrast, submicron monophased MnS particles were observed in the base metal (Fig. 3B). In the HAZ, large, chain-like MnS inclusions with preexisting micro-crevices and voids were commonly observed (Figs. 3C, 3G–3I). These chain-like manganese sulfide inclusions were along the rolling direction and could be 200 micrometers long.

Depth profiles of voids surrounding inclusions were measured and recorded by confocal laser scanning microscopy (CLSM) before and after corrosion immersion tests, as illustrated in Fig. 4. For the weld root pass metal, shallow, trench-like features were observed before corrosion testing (Figs. 4A–E). After corrosion immersion, some voids in the weld metal expanded or deepened (Figs. 4H–I); some voids around smaller inclusions did not show many changes (Figs. 4F and G). This observation also highlights that pits may not initiate at MnS inclusions smaller than 0.7 μm diameter in the weld metal. Previous research explored the relationships between inclusion size and the occurrence of pitting in stainless steel. Ke and Alkire (Refs. 32, 33) proposed that the pits did not initiate at MnS inclusions smaller than 0.7 μm. The rationale was that local S and Cl species concentrations did not surpass the critical values required for passivity breakdown. Stewart et al. (Ref. 34) reported that individual sulfides below a certain size, likely 0.5 μm, were too small

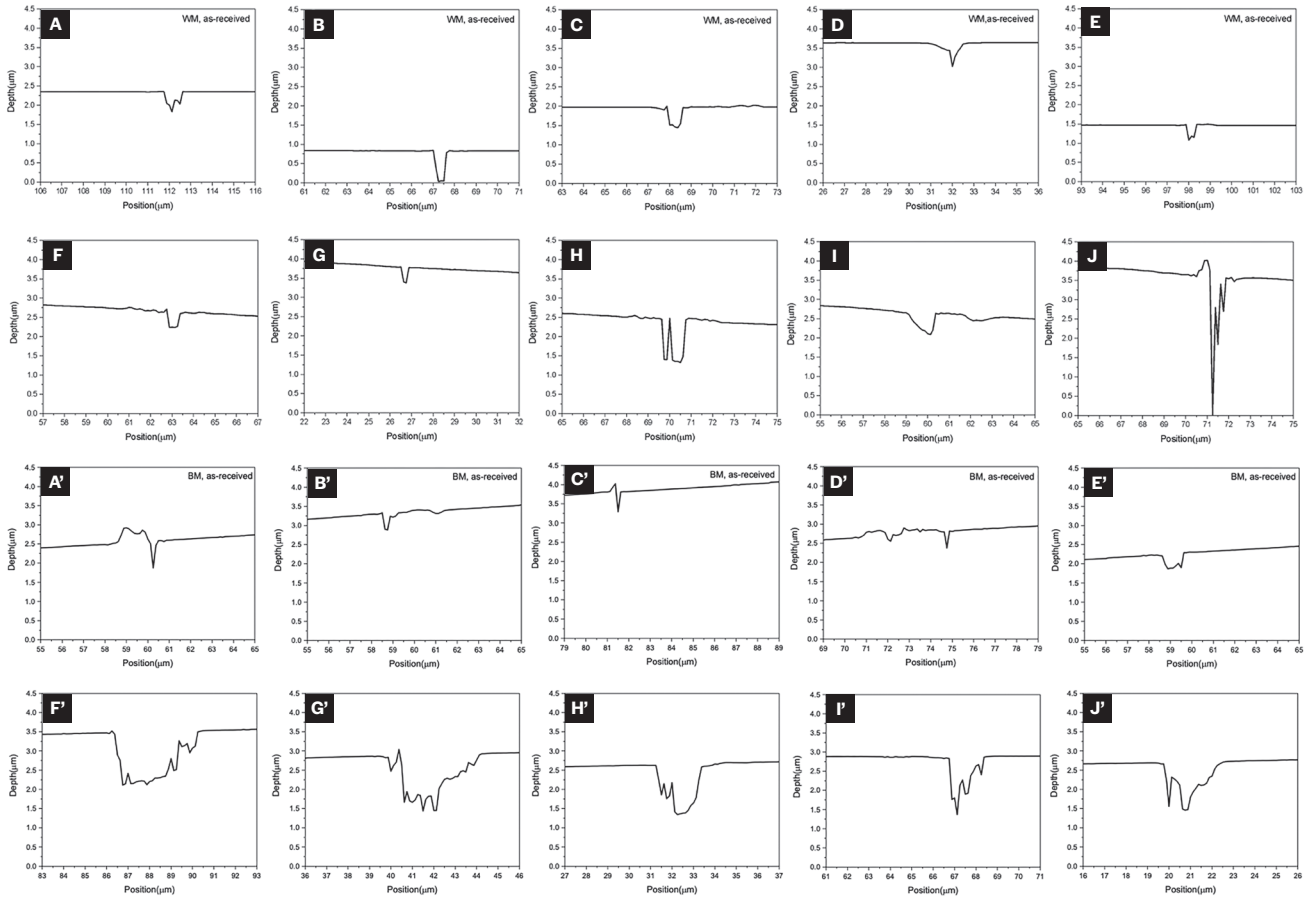


Fig. 4 – Depth profiles of the voids and corrosion pits measured by confocal laser scans: A–E – Root-pass weld metal voids before corrosion testing; F–J – root-pass weld metal voids after corrosion immersion test; A’–E’ – base metal voids before corrosion testing; F’–J’ – base metal voids after corrosion testing.

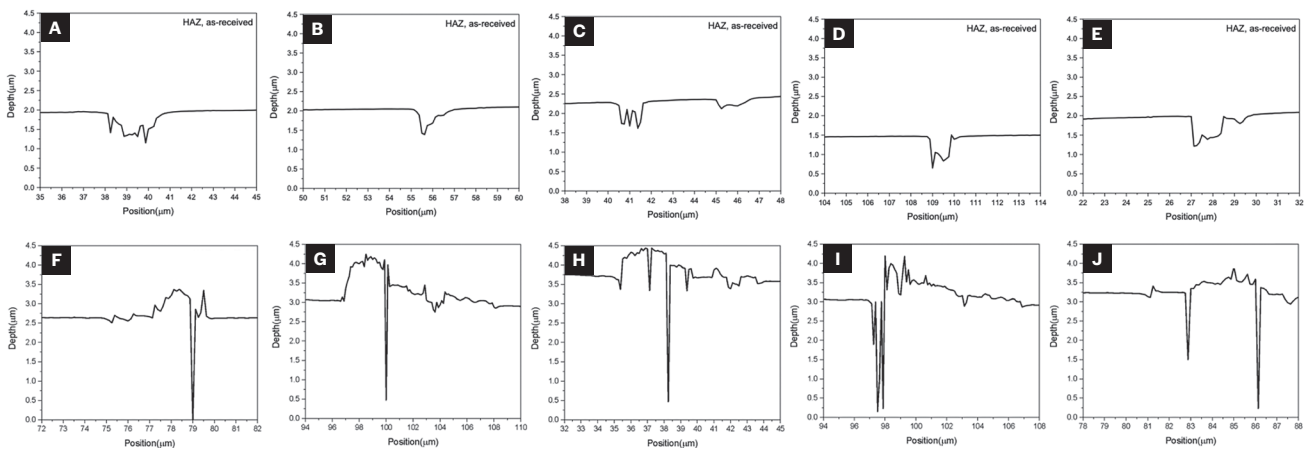
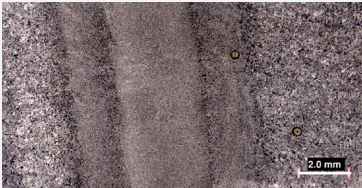
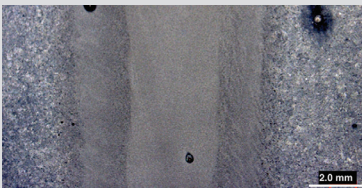


Fig. 5 – Depth profiles of the void's corrosion pits measured by confocal laser scans: A–E – Voids in the heat-affected zone before corrosion testing; F–J – pits in the heat-affected zone after corrosion testing.

to nucleate a damaging pit. Webb et al. (Ref. 35) observed that small and shallow MnS inclusions might trigger metastable corrosion. In contrast, large and deeply buried MnS inclusions resulted in narrow micro-crevices at the boundary with the steel matrix, inducing stable pitting corrosion by

maintaining thiosulfate and chloride concentrations above critical levels. Additionally, Yang et al. (Ref. 36) reported that the average pitting potential decreased with an increase in the average size of MnS inclusions, elevating susceptibility to pitting corrosion for pure industrial iron.

Table 2 — Girth Weld Internal Diameter Surface after Corrosion Immersion Tests

Pits distribution morphology	Corrosion pits density (counts/mm ²)		
	WM	HAZ	BM
	0	0.027	0.020
	0	0.12	0.082
	0	0.12	0.092
	0.026	0.077	0.065

In the base metal, voids around the inclusions before corrosion testing were shallow (Figs. 4A–E). After corrosion immersion, significant deepening happened to the voids (Figs. 4F–J). The shape of the voids seems to suggest that the MnS particles fell off, leaving behind cavities similar to the shapes of the inclusions.

The depth profiles of voids in the HAZ before corrosion testing are shown in Figs. 5A–E. Void profiles in the HAZ after corrosion testing are shown in Figs. 5F–J. Notably, voids in the HAZ were the deepest and sharpest among all weld joint regions, approximately twice as large as those in the weld metal and base metal. The typical pit morphology in the heat-affected zone after the corrosion testing is shown in Figs. 6A–C. As shown in Figures 6D–F, to reveal the grain boundaries, a 2% nital solution was applied to slightly etch. The corrosion pits were initiated at the inclusion/matrix boundaries but not on the grain boundaries.

Discussion

Al₂O₃ and MnS inclusions in the HAZ

At a lower magnification, the inclusion morphology in the heat-affected zone is the chain-like MnS clusters. Figure 7 illustrates the features and crystal microstructure surrounding these clustered MnS inclusions. The chain-like manganese sulfide clusters abutting the fusion line extend approximately 200 μm in length parallel to the rolling direction (Fig. 7B). At some sites of the inclusion/matrix interface, the boundaries exhibit voids, as indicated by the arrow in Fig. 7C, pointing to an alumina particle identified next. Even after Xe ion beam polishing, removing around 0.6 μm thickness of metal from this selected region, voids persisted (Fig. 7F). It is noted that no voids were observed along the MnS/matrix interface.

The region that the arrow is pointing toward in Fig. 7C was imaged using a high-resolution scanning electron microscope (HR-SEM). Focused ion (Ga) beam (FIB) sputtering was used to reveal a depth cross section, as depicted in Fig. 8. The in-situ EDS mappings (Fig. 8C) indicated that the rod-like MnS inclusion engulfed an alumina particle. It has been estab-

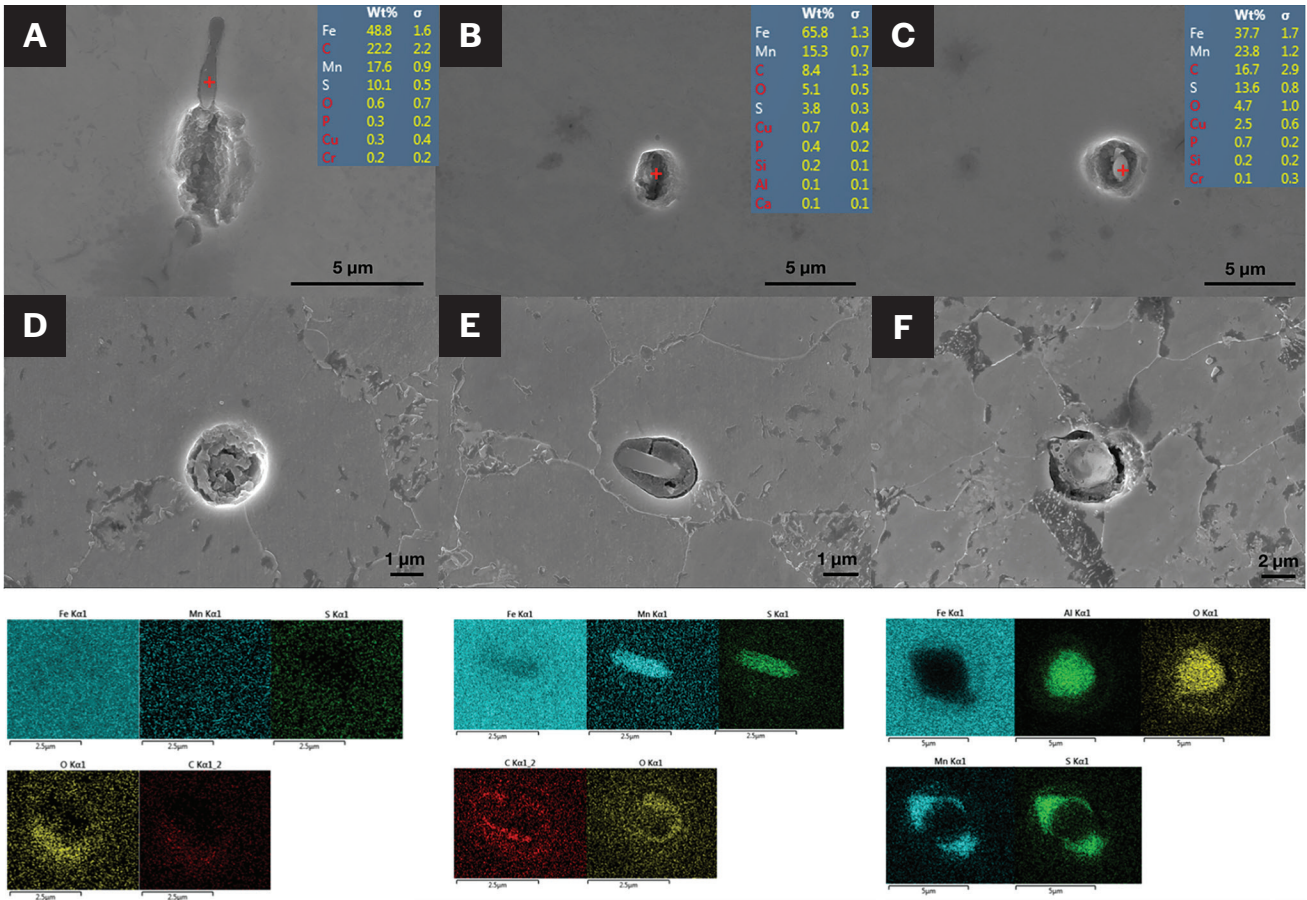


Fig. 6 – Typical pits in the heat-affected zone after corrosion testing: A–C – As-corrosion tested condition; D–F – lightly etched with 2% nital etchant to reveal the grain boundaries. The EDS mapping of the three inclusions.

Table 3 – EDS Point Analysis Results of Locations Labeled in Fig. 3 (wt-%)

Position	Mn	Si	Al	S	Cu	O	Fe
1	6.4	2.7	1.0	0.6	0.1	9.0	Bal.
2	6.4	3.0	1.0	0.2	0.1	9.2	Bal.
3	5.1	0.8	0.7	0.1	0.1	6.0	Bal.
4	3.1	1.6	0.7	0.1	0.1	5.2	Bal.
5	0.9	0.2	0.0	0.0	0.2	0.1	Bal.

lished in the literature that Al_2O_3 solid particles, with a higher melting point, provide effective heterogeneous nucleation sites for MnS precipitation during hot working (Refs. 37–40).

Figure 9 shows the solidification sequence for the base metal steel predicted by Thermo-Calc. Al_2O_3 is the first solid phase to appear at about 1850°C. MnS is the second solid

phase to appear at about 1400°C. Al_2O_3 particles will serve as the nucleation sites for MnS to precipitate. This prediction explains the coexistence of Al_2O_3 and MnS and agrees with the study by Kimura et al. (Ref. 39) that in low-carbon Mg-killed steel, MnS inclusions precipitate on oxide particles as triangular or rodlike particles when undercooled to 1500–1200 K.

Inclusion Coarsening in the HAZ

MnS undergoes a significant growth in the coarse-grained heat-affected zone. To explain this observation, we have developed a diffusion-based one-dimensional model, as depicted in Fig. 10. The size of the entire domain was set as 10 μm , comprising the phases MnS and austenite (γ). Given that the size of MnS in the base metal is submicron (close to 1 μm in diameter), the initial size of the MnS was set at 0.5 μm . The governing equations 1, 2, and 3 were solved using the finite difference method. The initial and boundary conditions for the model were as follows: The concentration of Mn in MnS (6.4%) was determined by the EDS measurement in Table 3; the nominal concentration of 1.41 wt-% Mn in the steel was set as the rightmost (far field) boundary condition for austenite; the concentration of Mn

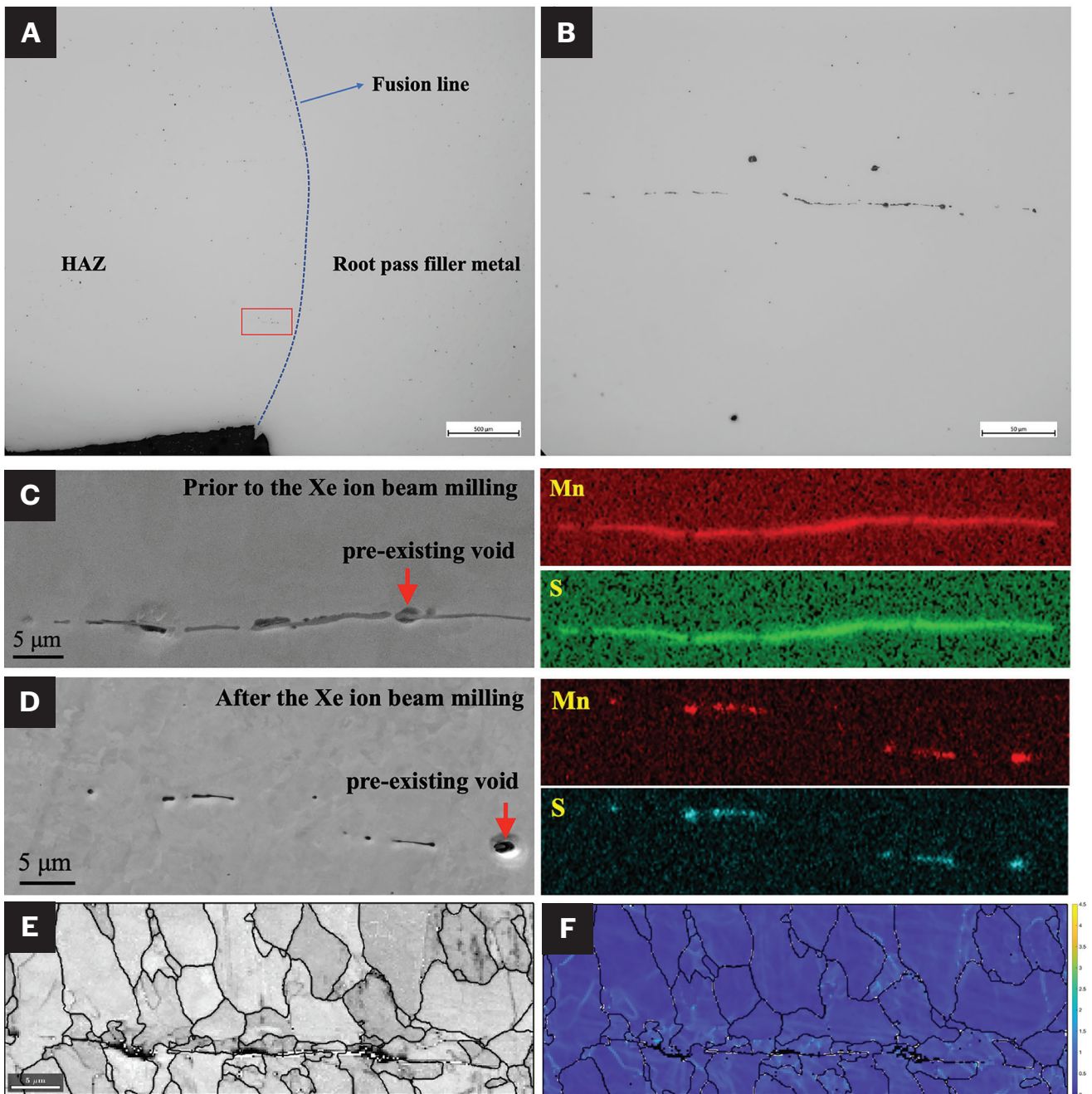


Fig. 7 – A – Optical micrograph showing the location of the region observed; B – higher magnification of the bracketed region showing a chain-like inclusion cluster; C – secondary electron image of the chain-like inclusion cluster; D – the chain-like inclusion cluster after Xe ion beam milling; E and F – grain boundary map and KAM map of the chain-like cluster region shown in C. Color maps are for Mn and S scans for regions shown in C and D, respectively.

at the MnS/austenite interface on the austenite side was calculated from Thermo-Calc at 1400°C as 1.04%. These boundary conditions are illustrated in the schematic in Fig. 10. While the HAZ region experienced a dynamic thermal history, for simplification purposes, we have assumed that the entire domain was subjected to a constant effective temperature of 1400°C for 2 s. The diffusion coefficient values of Mn in austenite were obtained from reference (Ref. 41). Considering that the diffusivity of Mn in austenite

is significantly lower than that of S, we have assumed Mn to be the limiting element for inclusion coarsening kinetics. It should be noted that the concentration gradient within the MnS is zero, and any binary eutectic that may form due to excess sulfur at the MnS/alloy interface is ignored. The concentration gradient across the MnS/ γ interface drives the growth or dissolution of the inclusion.

In the MnS region, $0 \leq x < S(t)$

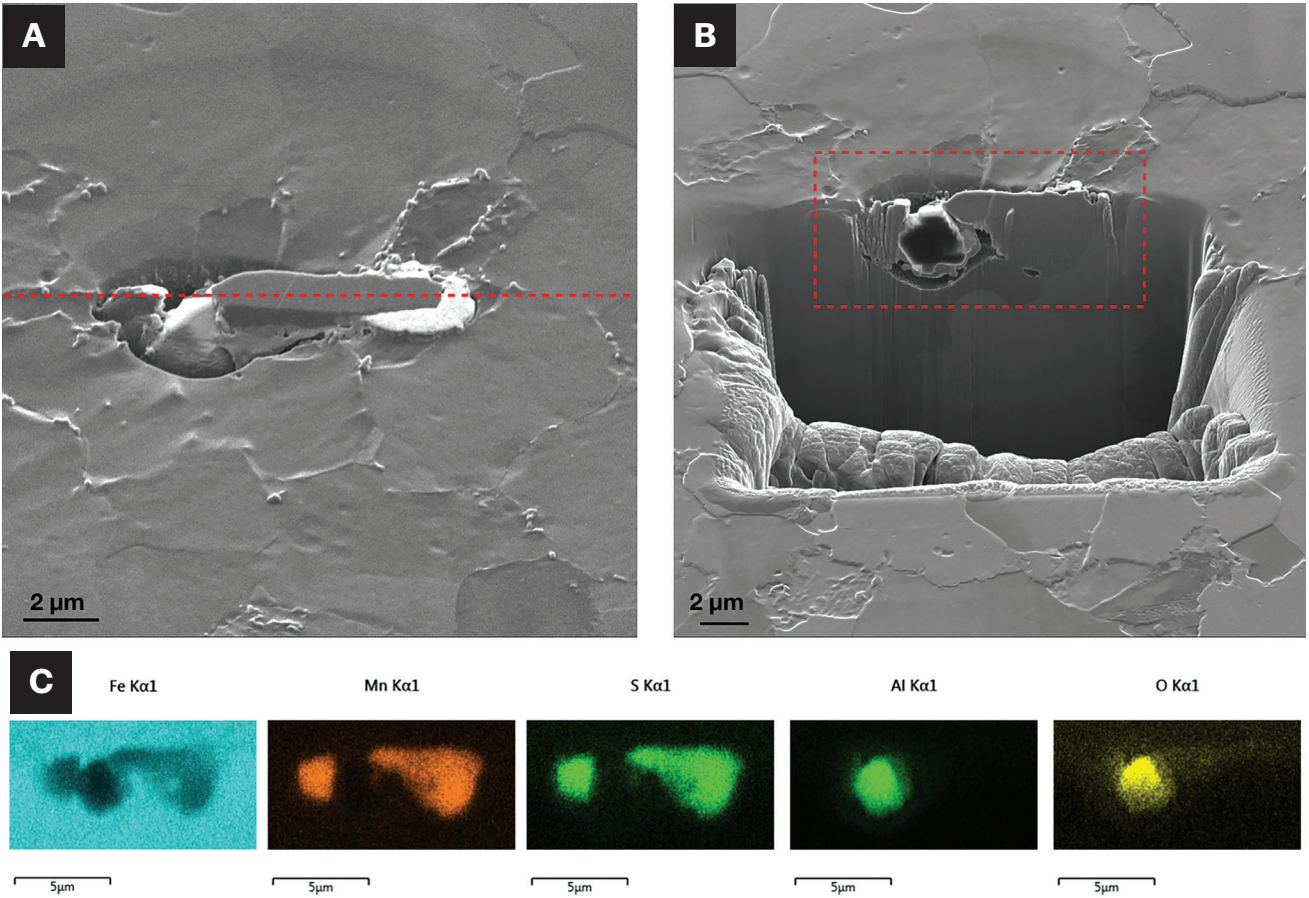


Fig. 8 – A – Top-down view; B – a cross-sectional view of the as-welded inclusion/matrix interfacial debonding in the HAZ region pointed to by the arrow in Fig. 7C; C – EDS mapping results of the selected rectangular region.

$$\frac{\partial C_{MnS}(x, t)}{\partial t} = D_{MnS} \frac{\partial^2 C_{MnS}(x, t)}{\partial x^2} \quad (1)$$

At Mn/S γ interface, $x = S(t)$

$$\begin{aligned} D_{MnS} \frac{\partial C_{MnS}^-}{\partial x} - D_{\gamma} \frac{\partial C_{\gamma}^{S+}}{\partial x} \\ = (C_{MnS}^{S+} - C_{\gamma}^{S-}) \frac{dS(t)}{dt} \end{aligned} \quad (2)$$

In γ region, $S(t) < x \leq L$

$$\frac{\partial C_{\gamma}(x, t)}{\partial t} = D_{\gamma} \frac{\partial^2 C_{\gamma}(x, t)}{\partial x^2} \quad (3)$$

where C is concentration, D is diffusion coefficient, S is interface location, x is distance, and t is time. As illustrated in Fig. 11, after 2 s, the size of MnS, represented by the position of

the MnS/ γ interface, increased from the initial 0.5 μm to 2.0 μm (4.0 μm in diameter). The SEM images in Fig. 3 also show that in the base metal, the size of MnS was 0.22 μm , but after the CGHAZ heat cycle, the MnS grew to a stringer morphology 0.42 μm wide and 5.9 μm in length. This is a direct observation of MnS growth in the CGHAZ region. This substantiates that MnS undergoes growth during the typical thermal cycles of the CGHAZ. The predicted size of MnS was smaller than the observed stringer-type MnS, which can be several hundred microns in length. This difference may be attributed to the observed MnS stringers growing along the rolling direction and following the path of the grain boundaries, where diffusion is much faster than in the bulk, resulting in larger-sized MnS. Additionally, when the growth of multiple MnS inclusions converges at the grain boundary, they may merge and eventually form the stringers. Besides the phase diagram predicting the dissolution of MnS on heating and regrowth on cooling, experimental evidence has been reported in the literature supporting the reprecipitation during cooling. For example, Glue et al. (Ref. 29) observed the original α - MnS particles dissolving during high-temperature (1100–1400°C) heat treatment. Upon cooling, sulfides were found to reprecipitate. Wang et al. (Ref. 42) observed MnS inclusions to grow in low-carbon steel with a low sulfur content of $\leq 0.035\%$. It must be noted

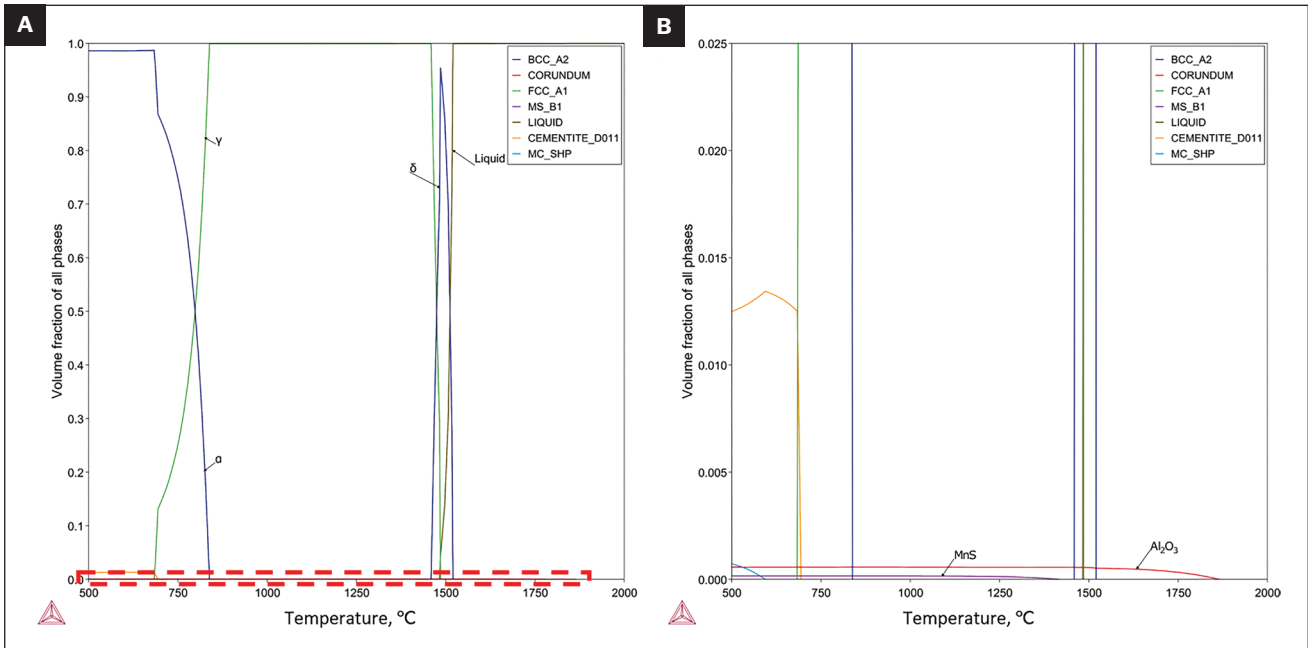


Fig 9 – A – The volume-fraction of all stable phases present in the considered low-carbon steam pipe as a function of temperature; B – The enlarged view of the area enclosed by the dashed rectangle in A.

again that the potential effect of binary eutectic at the MnS/ alloy interface has not been considered in this model.

A Debonding Mechanism for Inclusions

A five-pass weld joint was built with a moving heat source to simulate the thermal history of a specific area in the HAZ. The temperature-dependent thermal-mechanical material properties, including specific heat, thermal conductivity, and coefficient of thermal expansion, were estimated using the material property module of Thermal-Calc. The moving source volume-heat boundary condition was modeled through a Fortran DFLUX subroutine, and the volume heat model was programmed based on Goldak’s heat source (Ref. 43):

$$q_f(x, y, z) = \frac{6\sqrt{3}Q}{abc\pi\sqrt{\pi}} \exp\left(-\frac{3(x-x_o)^2}{a^2} - \frac{3(y-y_o)^2}{b^2} - \frac{3(z-z_o)^2}{c^2}\right) \quad (4)$$

$Q = 1338\text{W}$ is the heat input based on the weld process specifications; a , b , and c are the parameters controlling the shape of the volume heat source ($a = 3.1\text{ mm}$, $b = 5\text{ mm}$, and $c = 3.2\text{ mm}$); and x_o , y_o , and z_o are the coordinates of the center of the heat source, which is a function of time and programmed in accordance with the element birthing sequence.

To explore the thermal-mechanical field of the CGHAZ, the temperature and stress response of the node indicated by the red dot in Fig. 12A, corresponding to the CGHAZ location, were extracted from the model. As shown in Fig. 12C,

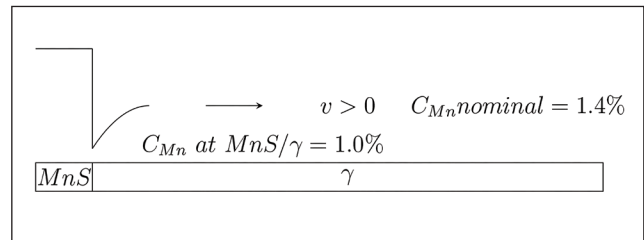


Fig. 10 – A schematic of the one-dimensional diffusion model for the growth of MnS during a welding thermal cycle. The velocity v of the MnS/ γ interface $S(t)$ is defined as $ds/(dt)$.

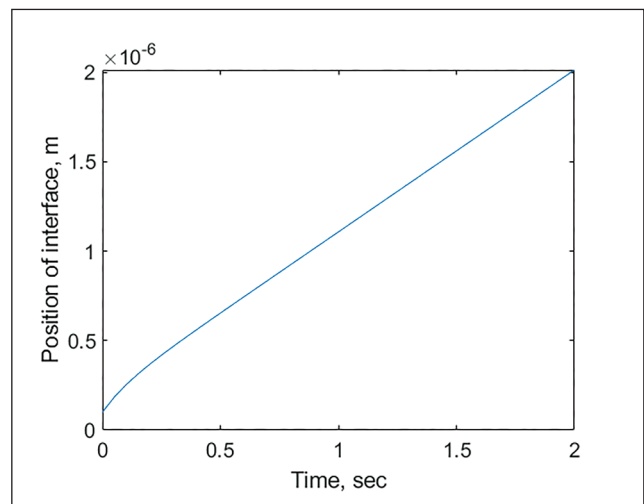


Fig. 11 – The position of MnS/ γ interface vs. time, predicting the size of MnS inclusion would grow fivefold at 1400°C isothermal condition for 2 s.

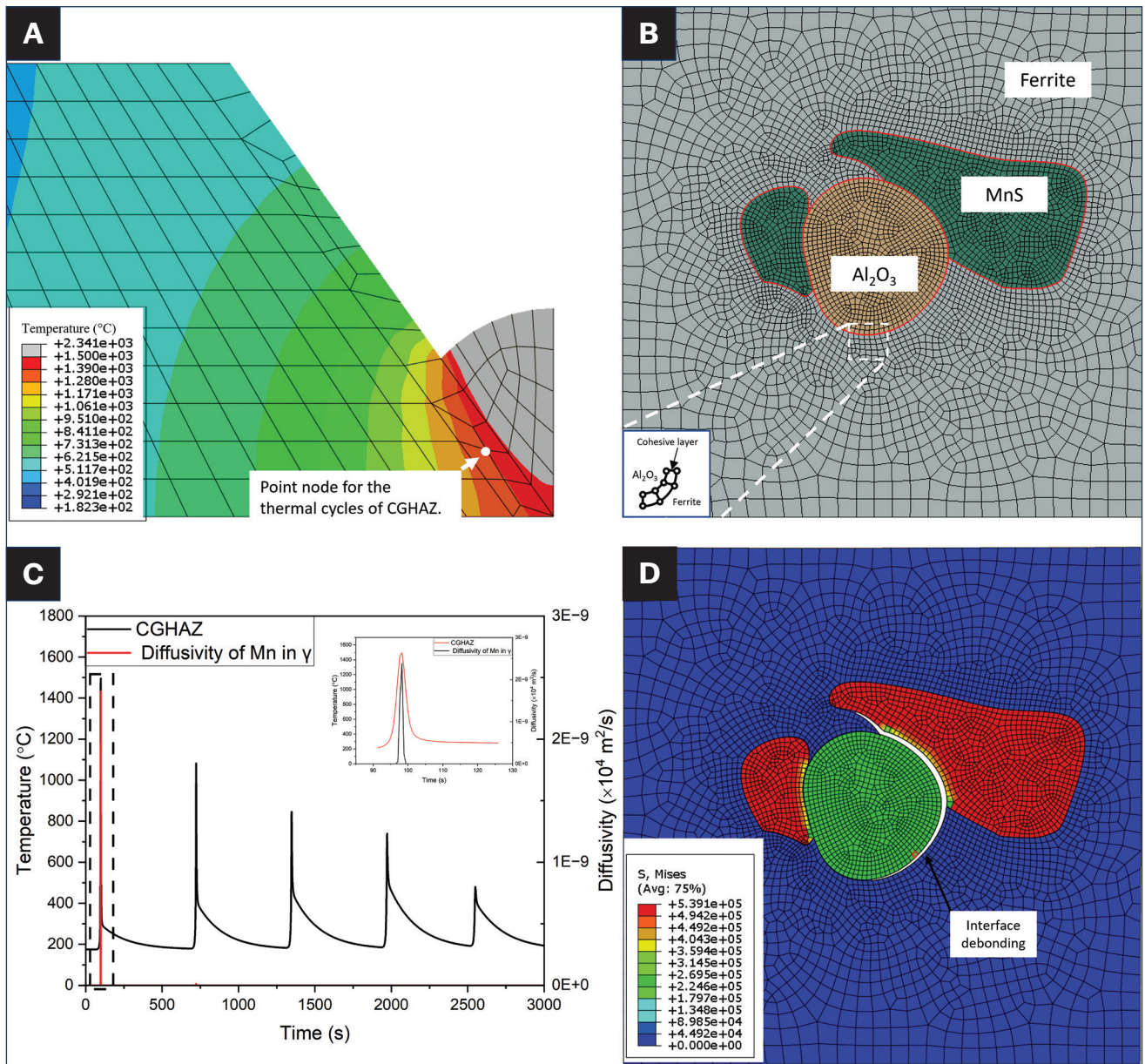


Fig. 12 – A – Predicted temperature field when the third welding pass is deposited. The white nodal point is used to extract the thermal cycles for the CGHAZ; B – the microstructure-scale model, with the red lines indicating the cohesive interface layer between particles; C – predicted thermal cycles for the CGHAZ in the 5-pass weld joint; D – predicted von Mises stress distribution after the first thermal cycle, showing the debonding has happened around the alumina (as indicated by the white line).

the peak temperature at CGHAZ of the first pass weld was significantly higher than the A_3 temperature, leading to grain coarsening and dissolution of precipitates. Although slightly lower, the peak temperature of the subsequent two thermal passes still surpassed the A_3 point. The macroscale model’s thermal history provides boundary conditions for the meso-scale computation, as shown in Fig. 12B, where a three-phase model was developed. The geometry was initially meshed with two-dimensional CPE4T plane-strain thermal-mechanical elements. Subsequently, a layer of cohesive elements with zero thickness was inserted between the MnS/matrix, MnS/ Al_2O_3 , and Al_2O_3 /matrix interfaces. Based on Liu et al. (Ref.

44), in the in-situ tensile loading experiment, the MnS would debond with the ferrite when the external loading reached a range of 150MPa–300MPa. Therefore, in this finite element model, the cohesive strength of the interface was set as 190 MPa, implying that the cohesive layer would degrade (fracture) and be deleted when its maximum principal stress exceeded 190 MPa.

Figure 12D illustrates the element stress and element status field after applying the heat cycle from the first welding pass. The interfaces of Al_2O_3 /ferrite and Al_2O_3 /MnS showed debonding, as evidenced by the absence of elements between the phases. The simulation underscored that the driving

force was sufficient to separate the Al_2O_3 /ferrite interface even after one thermal cycle. In comparison with the thermal expansion coefficient of the ferrite matrix ($1.5\text{E}-5/\text{K}$), that of MnS is slightly larger ($1.8\text{E}-5/\text{K}$), while that of Al_2O_3 is lower ($0.8\text{E}-5/\text{K}$) (Ref. 45). Consequently, the strain mismatch between Al_2O_3 and MnS is most pronounced during thermal cycles, leading to the highest thermal stresses. This finite element model suggests that owing to the coefficient of thermal expansion mismatch between the ferrite matrix and inclusion clusters, the inclusions/matrix interfaces in the CGHAZ will debond during welding thermal cycles. After the initial welding thermal cycle, interfacial debonding may happen due to incompatible deformation, separating the primitive atomic bonding between nonmetallic inclusions and the iron matrix. Although these separated interfaces may reattach during subsequent heating, the attachment is due to weak bonds (Ref. 46). Therefore, the formation of cavities and crevices is assumed at these weak-bonded interfaces (Refs. 46, 47). Furthermore, interfacial rebonding needs a high temperature, approaching the inclusion's dissolution temperature (over 1750°C for alumina). Such temperatures are unattainable in the heat-affected zone of multipass welds.

Conclusions

The heat-affected zone was found to have more pitting damage than the base metal and the weld fusion zone. The stringer-like inclusion clusters in the heat-affected zone were identified as MnS-engulfing Al_2O_3 particles. Interfacial debonding was found to be more likely to occur at the Al_2O_3 -MnS cluster interface. This debonding might have triggered the formation of voids or crevices at the inclusion and matrix interfaces before the workpiece entered the corrosion service. Thus, pitting damage was significantly enhanced by these crevices in the heat-affected zone. This proposed mechanism offers a potential explanation for the selective reactivity of sulfides, suggesting the likelihood that only sulfides clustering with oxides will function as active pitting initiation sites.

References

1. DeGarmo, E. P., Black, J. T., and Kohser, R. A. 2003. *Materials and Processes in Manufacturing*. Wiley.
2. Oberg, E., Jones, F. D., Horton, H. L., and Ryffel, H. H. 1988. *Machinery's Handbook: A Reference Book for the Mechanical Engineer, Designer, Manufacturing Engineer, Draftsman, Toolmaker and Machinist*. Industrial Press.
3. Smith, W. F., and Hashemi, J. 2006. *Foundations of Materials Science and Engineering*. McGraw Hill.
4. Kain, V. 2014. Flow accelerated corrosion: Forms, mechanisms and case studies. *Procedia Engineering* 86: 576–588.
5. Kain, V., Roychowdhury, S., Mathew, T., and Bhandakkar, A. 2008. Flow accelerated corrosion and its control measures for the secondary circuit pipelines in Indian nuclear power plants. *Journal of Nuclear Materials* 383(1): 86–91.
6. Kain, V., Roychowdhury, S., Ahmedabadi, P., and Barua, D. K. 2011. Flow accelerated corrosion: Experience from examination of components from nuclear power plants. *Engineering Failure Analysis* 18(8): 2028–2041.

7. Port, R. D. 1998. Flow accelerated corrosion. *NACE Conference Papers* 98721.
8. Fontana, M. G. 2005. *Corrosion Engineering (3rd ed)*. New Delhi: McGraw Hill.
9. Islam, Md. A., and Farhat, Z. 2017. Erosion-corrosion mechanism and comparison of erosion-corrosion performance of API steels. *Wear*: 376–377, 533–541.
10. Saini, N., Wang, Y., and Li, L. 2022. Failure analysis of once-through steam generator (OTSG) external piping welds. *Journal of Failure Analysis and Prevention* 22(3): 1180–1195.
11. Zeng, L., Chen, G., and Chen, H. 2020. Comparative study on flow-accelerated corrosion and erosion-corrosion at a 90° carbon steel bend. *Materials* 13(7): 1780.
12. Ahmed, W. H. 2010. Evaluation of the proximity effect on flow-accelerated corrosion. *Annals of Nuclear Energy* 37(4): 598–605.
13. El-Gammal, M., Mazhar, H., Cotton, J. S., Shefski, C., Pietralik, J., and Ching, C. Y. 2010. The hydrodynamic effects of single-phase flow on flow accelerated corrosion in a 90° -degree elbow. *Nuclear Engineering and Design* 240(6): 1589–1598.
14. Ahmed, W. H., Bello, M. M., El Nakla, M., and Al Sarkhi, A. 2012. Flow and mass transfer downstream of an orifice under flow accelerated corrosion conditions. *Nuclear Engineering and Design* 252: 52–67.
15. Tomarov, G. V., and Shipkov, A. A. 2018. Flow-accelerated corrosion wear of power-generating equipment: Investigations, prediction, and prevention: 1. Flow-accelerated corrosion processes and regularities. *Thermal Engineering* 65(8): 493–503.
16. Fredj, N., Burleigh, T. D., Heidersbach, K. L., and Crowder, B. R. 2012. Corrosion of carbon steel in waters of varying purity and velocity. *NACE International Corrosion Conference Series* 5.
17. Karaminezhad-Ranjbar, M., Mankowski, J., and Macdonald, D. D. 1985. Pitting corrosion of Inconel 600 in high temperature chloride solution under controlled hydrodynamic conditions. *Corrosion* 41 (4): 197–204.
18. Wang, Y., Li, L., Lyu, Z., Saini, N., and Wu, Z. 2023. Flow-accelerated corrosion damage in a steam pipe girth weld. *Journal of Materials Engineering and Performance* 32(8): 3796–3808.
19. Wranglen, G. 1974. Pitting and sulphide inclusions in steel. *Corrosion Science* 14(5): 331–349.
20. Lin, B., Hu, R., Ye, C., Li, Y., and Lin, C. 2010. A study on the initiation of pitting corrosion in carbon steel in chloride-containing media using scanning electrochemical probes. *Electrochimica Acta* 55(22): 6542–6545.
21. Chiba, A., Muto, I., Sugawara, Y., and Hara, N. 2013. Pit initiation mechanism at MnS inclusions in stainless steel: Synergistic effect of elemental sulfur and chloride ions. *Journal of The Electrochemical Society* 160(10): C511.
22. Muto, I., Kurokawa, S., and Hara, N. 2009. Microelectrochemical investigation of anodic polarization behavior of CrS inclusions in stainless steels. *Journal of The Electrochemical Society* 156(11): C395.
23. Nishimoto, M., Muto, I., Sugawara, Y., and Hara, N. 2019. Morphological characteristics of trenching around MnS inclusions in Type 316 stainless steel: The role of molybdenum in pitting corrosion resistance. *Journal of The Electrochemical Society* 166(11): C3081–C3089.
24. Zhao, X. H., Sheng, Y. X., Yin, C. X., Li, G. F., and Han, Y. 2016. Effects of Cl⁻ concentration on corrosion behavior of carbon steel and super13Cr steel in simulated oilfield environments. *Proceedings of the 2016 International Conference on Innovative Material Science and Technology (IMST 2016)*.
25. Zhang, G. A., and Cheng, Y. F. 2011. Localized corrosion of carbon steel in a CO_2 -saturated oilfield formation water. *Electrochimica Acta* 56(3): 1676–1685.

26. Bai, Z. Q., Chen, C. F., Lu, M. X., and Li, J. B. 2006. Analysis of EIS characteristics of CO₂ corrosion of well tube steels with corrosion scales. *Applied Surface Science* 252 (20): 7578–7584.
27. Furuseth, S., Kjekshus, A., Niklasson, R. J. V., Brunvoll, J., and Hinton, M. 1965. On the properties of alpha-MnS and MnS₂. *Acta Chemica Scandinavica* 19: 1405–1410.
28. Diederichs, R., and Bleck, W. 2006. Modelling of manganese sulphide formation during solidification, Part I: Description of MnS formation parameters. *Steel Research International* 77(3): 202–209.
29. Glue, D. R., Jones, C. H., and Lloyd, H. K. M. 1975. Effect of composition and thermal treatment on the overheating characteristics of low-alloy steels. *Metals Technology*.
30. Temmel, C., Ingesten, N. G., and Karlsson, B. 2006. Fatigue anisotropy in cross-rolled, hardened medium carbon steel resulting from MnS inclusions. *Metallurgical and Materials Transactions A* 37(10): 2995–3007.
31. Brooksbank, D., and Andrews, K. W. 1972. Stress fields around inclusions and their relation to mechanical properties. *Production and Application of Clean Steels*: 186–198.
32. Ke, R. and Alkire, R. 1995. Initiation of corrosion pits at inclusions on 304 stainless steel. *Journal of the Electrochemical Society* 142, 4056.
33. Ke, R., and Alkire, R. 1992. Surface analysis of corrosion pits initiated at MnS inclusions in 304 stainless steel. *Journal of the Electrochemical Society* 139(6): 1573–1580.
34. Stewart, J., and Williams, D. E. 1992. The initiation of pitting corrosion on austenitic stainless steel: On the role and importance of sulphide inclusions. *Corrosion Science* 33(3): 457–474.
35. Webb, E. G., Suter, T., and Alkire, R. C. 2001. Microelectrochemical measurements of the dissolution of single MnS inclusions, and the prediction of the critical conditions for pit initiation on stainless steel. *Journal of the Electrochemical Society* 148(5): B186.
36. Yang, S., Zhao, M., Feng, J., Li, J., and Liu, C. 2018. Induced-pitting behaviors of MnS inclusions in steel. *High Temperature Materials and Processes* 37(9–10): 1007–1016.
37. Oikawa, K., Ohtani, H., Ishida, K., and Nishizawa, T. 1995. The control of the morphology of MnS inclusions in steel during solidification. *ISIJ International* 35(4): 402–408.
38. Yuki, N., Shibata, H., and Emi, T. 1998. Solubility of MnS in Fe–Ni alloys as determined by in-situ observation of precipitation of MnS with a confocal scanning laser microscope. *ISIJ International* 38(4): 317–323.
39. Kimura, S., Nakajima, K., Mizoguchi, S., and Hasegawa, H. 2002. In-situ observation of the precipitation of manganese sulfide in low-carbon magnesium-killed steel. *Metallurgical and Materials Transactions A* 33(2): 427–436.
40. Tanaka, Y., Pahlevani, F., Moon, S. C., Dippenaar, R., and Sahajwalla, V. 2019. In situ characterisation of MnS precipitation in high carbon steel. *Scientific Reports* 9(1): 10096.
41. Choudhary, S. K., and Ghosh, A. 2009. Mathematical model for prediction of composition of inclusions formed during solidification of liquid steel. *ISIJ International* 49(12): 1819–1827.
42. Wang, F., Guo, H., Liu, W., Yang, S., Zhang, S., and Li, J. 2019. Control of MnS inclusions in high- and low-sulfur steel by tellurium treatment. *Materials* 12(7): 1034.
43. Goldak, J., Chakravarti, A., and Bibby, M. 1984. A new finite element model for welding heat sources. *Metallurgical Transactions B* 15(2): 299–305. DOI: 10.1007/BF02667333
44. Liu, X., Wang, C., Gui, J., Xiao, Q., and Guo, B. 2019. Effect of MnS inclusions on deformation behavior of matrix based on in-situ experiment. *Materials Science and Engineering: A* 746: 239–247.
45. Otsuka, T., Hanada, H., Nakashima, H., Sakamoto, K., Hayakawa, M., Hashizume, K., and Sugisaki, M. 2005. Observation of hydrogen distribution around non-metallic inclusions in steels with tritium microautoradiography. *Fusion Science and Technology* 48(1).
46. Mirzayev, D. A., Fominykh, E. A., Tokovoi, O. K., Vorob'ev, N. I., Shaburov, D. V., and Yakovleva, I. L. 2007. Scanning electron microscopy of the flake structure in the forgings of structural alloy steel containing 0.4% carbon. *The Physics of Metals and Metallography* 103(3): 292–298.
47. Laureys, A., Pinson, M., Claeys, L., Deseranno, T., Depover, T., and Verbeke, K. 2020. Initiation of hydrogen induced cracks at secondary phase particles. *Frattura ed Integrità` Strutturale* 14(52): 113–127.

YAJING WANG, ZHE LYU, and LEIJUN LI (*leijun@ualberta.ca*) are with the Department of Chemical & Materials Engineering, University of Alberta, Edmonton, Alberta, Canada. **ZHISHENG WU** and **WANG** are with the School of Materials Science and Engineering, Taiyuan University of Science and Technology, Taiyuan, Shanxi, China. **WANG** is also with the Department of Chemistry and Chemical Engineering, Lvliang University, Lvliang, Shanxi, China.